New trends in infrared detectors technology

A. ROGALSKI

Institute of Technical Physics, Military University of Technology
01-489 Warszawa, Poland

1. Introduction

Recent efforts in the technology of infrared detectors have been mostly concentrated on large electronically scanned focal plane arrays (FPAs). The increased sensitivity, resolution and reduction in system complexity of FPAs offer significant advantages in military as well as civil applications in thermal imaging, guidance, reconnaissance, surveillance, ranging and communications systems. It results from fundamental consideration that HgCdTe is the most important semiconductor alloy for manufacturing infrared detectors which can operate in the spectral range $1 \div 25$ μm. HgCdTe detectors as the intrinsic photon detectors absorb the IR radiation across the fundamental energy gad and are characterized by high optical absorption coefficient and quantum efficiency, and relatively low thermal generation rate comparing to extrinsic detectors and silicide Schottky barriers. The operating temperature for intrinsic detectors is, therefore, higher than for other types of photon detectors.

Fig. 1 shows, according to Elliott calculations [1], the temperature required for backgroung limited operation in 30° field of view as a function of cut-off wavelength. The lower line is *n*-type HgCdTe photoconductive material with a net donor concentration $N_d = 3 \cdot 10^{14}$ cm^{-3}. For comparison, the experimental results provided by Charlton are included. Shockley-Read-Hall (SRH) generation was omitted from calculation which includes Auger and radiative generation. The poorer agreement at shorter wavelengths reflects the neglect of SRH generation. A theoretical plot more appropriate to *n*-on-*p* diodes, where bulk of the generation volume is *p*-type, is also shown in the case of an acceptor concentration of 10^{16} cm^{-3}.

It results from Fig. 1 that HgCdTe detectors with background limited performance operate with thermoelectric coolers in

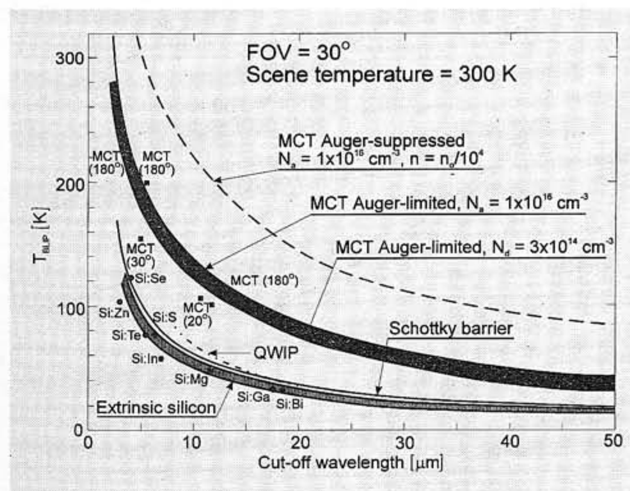

Fig. 1. Estimates of the temperature required for background limited operation of different types of photon detectors, plotted versus 30°, full cone angle except where indicated. The scene temperature is 300 K. The theoretical line and experimental points for extrinsic silicon are taken from *Sclar* (Prog. Quantum Electron., 9, 1984, p. 149). The experimental data on HgCdTe photoconductive detectors was supplied by *Charlton* (after Ref. [1])

MWIR range, instead of LWIR detectors at approximately 90 K. These attributes translate to the flexibility and capability to produce short wavelength infrared (SWIR), medium wavelength infrared (MWIR) and long wavelength infrared (LWIR) detectors. However, HgCdTe creates the most serious technological problems of any semiconductor material in mass production. The material is difficult to grow, and devices are expensive and power-consumptive. In spite of the achievements in material and device quality, difficulties still exist due to lattice, surface, and interface instabilities, i.e. it can sustain a large variation in stoichimetry and transport properties as a results of treatments as diverse as oxidation, mechanical damage, and reaction with metals. The difficulties with this material have made it desirable to examine other material systems to see whether performance can be improved.

It seems that the most important aim in infrared detector technology is to make detectors cheaper and more convenient in use. Cooling requirements make higher the cost, bulk, weight, power cosumption and inconvenience of IR systems. In contrary, the uncooled detectors are lightweighting, small and convenient to use. The present uncooled and near-room temperature detectors are essentially sub-BLIP detectors [$1 \div 4$].

This paper is concerned the new trends in infrared detector technology. We will concentrate principally on two groups of detectors: photon detectors (silicide Schottky barriers, quantum well detectors and ways to improve the performance of near-room temperature detectors) and thermal detectors (pyroelectric detectors and bolometers). However, at the beginning of the paper a short outlook of trends in HgCdTe photodiode technology will be done.

2. HgCdTe photodiodes

The design of hybrid HgCdTe FPAs is currently based on junction photodiodes, due to reduced electrical power dissipation, high impedance matched directly into the imput stage of a silicon CCD, and less stringent noise requirements for the readout devices and circuits [5]. Hitherto, the realization of HgCdTe photodiodes has been usually based on an *n*-on-*p* structure with base *p*-type maaterial with carrier concentration of the order of 10^{16} cm^{-3}. Theoretical reasons for the choice of the *n*-on-*p* configuration include the significantly longer minority carrier diffusion length in *p*-type material and the possibility of achieving longer minority carrier lifetime in *p*-type material rather than in a *n*-type one of comparable carrier concentration. The most common technique for producing n^+-*p* junctions is by ion implanatation into a *p*-type material Usually however, *p*-type material is characterized by relatively high trap concentration, which dominates the excess carrier lifetime by the Shockley-Read-Hall recombination mechanism.

In 1985, Rogalski and Larkowski [6] indicated that due to lower mobility of holes in *n*-type region of p^+-*n* junctions with thick *n*-type region, diffusion limited R_0A product of such junctions is larger than for n^+-*p* ones. The above theoretical predictions have been recently confirmed by experimental results obtained for p^+-*n* HgCdTe junctions [$7 \div 12$]. One

important advantage of the p-on-n device is that the n-type HgCdTe carrier concentration is easy to control in the $10^{14} \div 10^{15}$ cm^{-3} range using extrinsic doping; while for n-on-p device, the control of p-type carrier concentration at these levels is difficult. Because of the lower carrier concentrations achieved in the n-type HgCdTe material, it has longer minority carrier lifetimes than in p-type base layers.

A schematic of mesa and planar double-layer heterojunction (DLHJ) structures used in fabrication of p-on-n HgCdTe photodiodes is presented in Fig. 2. The n-type base, which is the absorbing region, has a thickness $10 \div 20$ μm and is deliberately doped with indium at a level of about $(1 \div 3) \cdot 10^{15}$ cm^{-3}. The composition of the base material is chosen for the wavelength of interest and for 10 μm radiation the composition $x = 0.225$. The p-n junction is formed using arsenic as the dopant at a level of about 10^{18} cm^{-3}. To acivate As as acceptor, it must occupy a Te side in the lattice. This requires either growth or annealing at relatively high temperatures under cation-rich conditions. Liquid phase epitaxy (LPE) growth from a Hg melt satisfies this condition automatically (although some postgrowth annealing may be required) [10]. Metalorganic chemical vapour deposition (MOCVD) [8] and molecular beam epitaxy (MBE) [9] have been successfully accomplished As doping growth. Arsenic has also been diffused from Hg solution [7] and from implants [8].

As shown in Fig. 2, p-type capping layers with composition $x_c > x_b$, have a thickness $1 \div 2$ μm. In these structures the built-in electric fields at heterojunction interfaces repel minority carriers and the R_oA product is enhanced. Thus R_oA product of double-layer heterojunction structure is higher than of homostructure. The electrical junction is positioned near the metallic interface and it is wise to place the junction in the small band gap layer to avoid deleteroius effects on the quantum efficiency and dark currents. This device operates as a homojuction with a small p-region placed in the small band gap of $\leqslant 1$ μm. Passivation of HgCdTe has been done by several techniques described in the comprehensive review by Nemirovsky and Bahir [13]. Recently, however, most laboratories use CdTe or CdZnTe (deposited by MBE, MOCVD, sputtering and electron-beam evaporation) for photodiode passivation [14]. It should be noticed, that photodiode passivation remains one of the most difficult and most proprietary of all aspects of current IR technology. Main issues appear to be adequate surface preparation, control of surface and film stoichiometry, deposition-induced surface damage, film integrity and dielectric strength, stability and suitability as an environment coating, adherence of subsequent metal depositions.

Wang's experimental results indicate that the performance of p-on-n and n-on-p photodiodes exhibit similar R_oA products at 77 K for $\lambda_c < 10$ μm. Instead for $\lambda_c > 10$ μm, the R_oA products of n-on-p photodiodes are generally inferior, their quantum efficiency is lower and the forward impedance is higher [11]. Wang suggests that these problems are probably caused by the relative immaturity in fabricating n-on-p heterojunctions, especially in the surface control on the p-side for diodes with a longer cutoff wavelength.

Recently, Rogalski et al. [15] have analyzed the performance of p^+-n-n^+ HgCdTe homojunction photodiodes with 20 μm thick base region. The effect of doping profiles on the photodiode performance (R_oA product, quantum efficiency) has been solved by forward condition steady-state analysis [16].

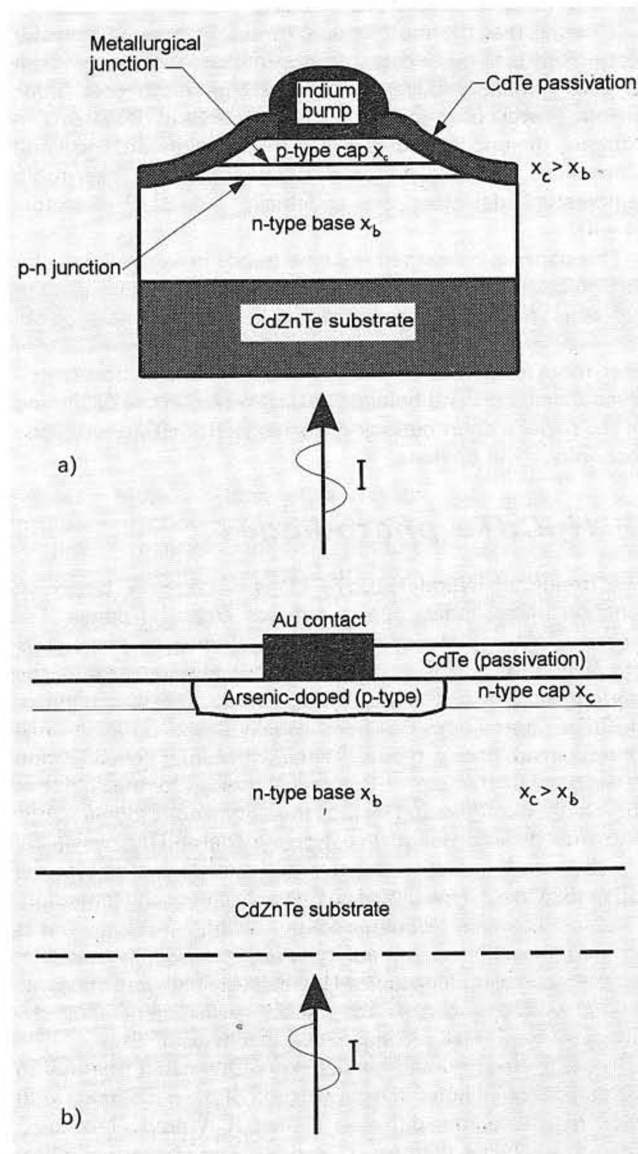

Fig. 2. Schematic cross section view of DLHJ mesa a) and planar b) LWIR HgCdTe diodes

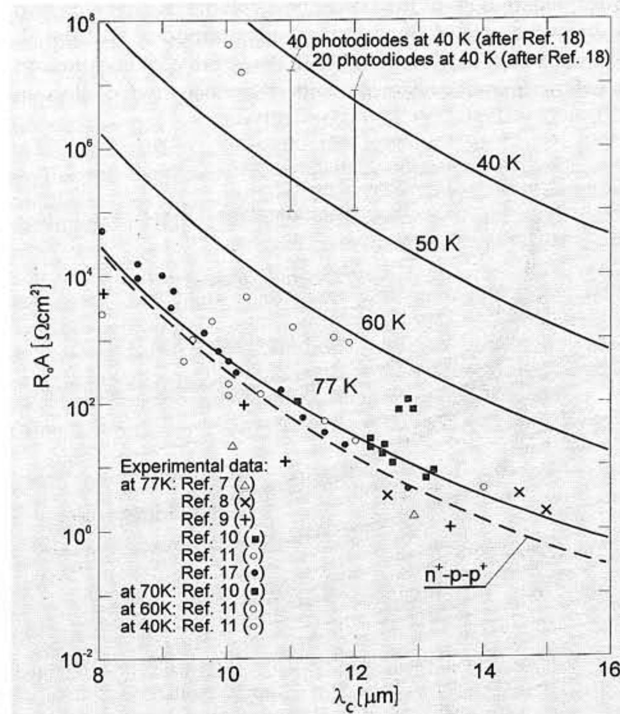

Fig. 3. Dependence of the R_oA product on the long wavelength cut-off for LWIR p^+-n-n^+ HgCdTe photodiodes at temperatures $\leqslant 77$ K. The theoretical lines are calculated assuming diffusion current mechanism. The experimental values are taken from Refs. [7÷11,17,18]

Fig. 3 shows the dependence of the R_oA product on the long wavelength cut-off for p^+-n-n^+ LWIR HgCdTe photodiodes at different temperatures. Theoretical curves are calculated assuming diffusion dark current. For comparison, the figure also shows theoretical curves for n^+-p-p^+ (the same geometry) photodiodes at 77 K with optimum acceptor concentration in p-type base region $N_a=10^{16}$ cm^{-3}. We can see that the last structure is inferior in comparison with p^+-n-n^+ one, especialy in more long-wavelength spectral range.

In Fig. 3 the experimental data reported by many authors for p^+-n-n^+ structures are also included. A satisfactory agreement between the theoretical curves and experimental data has been achieved for the temperature range 77÷60 K. The experimental data according to Ref. [10] very good agrees with theoretical calculations. Several experimental points [17] for temperature 77 K in the wavelength range $7<\lambda_c<10$ μm are located above the theoretical curve. Such experimental data obtained in the Santa Barbara Research Center, concern photodiodes manufactured with HgCdTe/CdTe heterostructures. In this case a gradient of x-composition in proximity of CdTe substrate can improve blocking properties of n-n^+ backside junction, which results in increasing R_oA product.

The discrepancy between theoretical curves and experimental data increases, with a lowering of the operation temperature of photodiodes. This is probably due to additional currents in the junctions (such as tunneling current or surface leakage current) which are not considered. It should be noticed that the upper experimental data at 40 K coincides very well with theoretical curve. However, this agreements is accidental since the experimental values were obtained for DLHJ mesa and planar structures (see Fig. 2). In these structures the built-in electric fields at heterojunction interfaces repel minority carriers and the R_oA product is enhanced. Thus theoretically predicted R_oA product for DLHJ structures is higher than shown in Fig. 3 for p^+-n-n^+ homojunction structures.

At present, the performance of HgCdTe FPAs are uniformity-limited. At 77 K, the operability of planar p-on-n heterostructures grown by MBE, determined by cumulative distribution functions for R_oA product, is ≥95%, but at 40 K the sport population limits the operability to 70÷80% [18]. The current mechanisms controlling the behavior at temperatures below 60 K are dominated by defects of unknown origin [19, 20]. Multistep recombination via these defects plus variations in local electrical parameters are probably the cause for not observing the expected strong band to band gap effects on devices, as evidenced in the 77 K data for the best arrays of photodiodes, where the currents are diffusion-limited. The specific electrically active defects which cause these deleterious effects are unknown, and their sources are likely to be numerous and diverse. This spread in values of R_oA product and limits applications of HgCdTe FPAs in low background conditions.

Up to the present, photovoltaic HgCdTe FPAs have been based on p-type material. Linear (240, 288, 480, and 960 elements), two-dimensional (2-D) scanning arrays with time delay and integration (TDI), and 2-D staring formats from 32×32 up to 480×640 have been made [17]. Pixel sizes ranging from 20 μm square to over 1 mm have been demonstrated. The best results have been obtained using hybrid architecture, which permits independent optimization of both the materials parameters and device fabrication processes for detectors and the signal-processing electronics (exploiting advances in CMOS manufacturing processes).

CdTe and CdZnTe are the most widely used substrates for backside-illuminated HgCdTe detector arrays. Their metallurgical compatibility permits the growth of very low defect density epitaxial layers of HgCdTe. However, the available substrates are relatively small, expensive, and fragile. Also thermal expansion mismatch between epitaxial layer and silicon causes a lateral ddisplacement of the detector and readout substrates when a hybrid FPA is cooled to its operating temperature, typically to 77÷120 K. On account of this, the largest hybrid FPAs fabricated with CdTe or CdZnTe detector substrates have 128×128 pixel formats.

To produce larger hybrid FPAs and to decrease their cost, alternative detector substrated have been used. In Rockwell's PACE-1 fabrication process [21, 22] inexpensive sapphire substrates (which thermal expansion mismatch to silicon is 40% less than that of CdTe) are used. In this process, a CdTe epitaxial layer is first grown by MOCVD, and next a p-type HgCdTe layer is grown from Te-rich melt using LPE. The p-n junctions are formed by boron-ion implantation in p-type material and subsequent thermal annealing. The planar junctions are passivated with a ZnS or CdTe film. In Table 1 the list of the performance of the PACE-1256×256 and 640×480 FPAs [23, 24] is given. The hybrid HgCdTe 256×256 FPAs offer TV-type resolution with ≈10 mK sensitivity at operating temperatures ≤130 K. Instead for 640×480 FPAs, $NE\Delta T$ of 0.015 K has been measured, what means that the sensitivity is nearly an order of magnitude higher than has been typically reported for the currently available PtSi 640×480 FPA technology. Chronological development of various FPA technologies in 3÷5 μm spectral region is compared in Fig. 4.

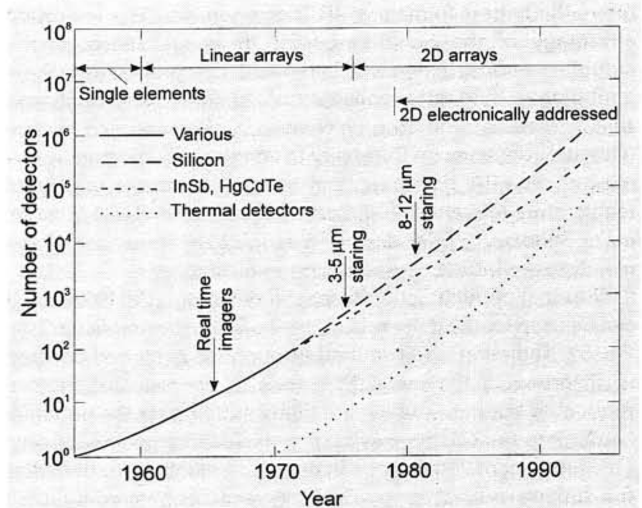

Fig. 4. An illustration of the increasing size of detector arrays with time. The line labelled silicon refers to both Schottky barriers and extrinsic silicon. The line labelled InSb and HgCdTe refers to both monolithic and hybrid technologies. The line labelled thermal detectors refers to both pyroelectric and bolometer detectors (after Ref. [1])

Table 1. **Large PACE-1 HgCdTe FPAs specifications (after Ref. [24])**

Parameter	256×256	640×480
Cell pitch [μm]	40	27
Chip package LLCC	68 pin	84 pin
Typical usable DR	$>10\cdot10^3$	$>5\cdot10^3$
MWIR NETD at $Q_b=3\cdot10^{14}$/cm^{2}s [mK]	<7	≤15
Responsivity nonuniformity (max : min)	<1.4 : 1	–
Pixel operability [%]	>98	–
Outputs	1(2)	4
Maximum data rate per output [MHz]	20	20
Minimum detectivity at $Q_b=3\cdot10^{14}$/cm^{2}s [10^{11} cmHz$^{1/2}$W^{-1}]	>5	>5
Transfer ratio [nV/e$^-$]	46	35

Infrared absorption by sapphire limits the use of PACE-1 FPAs to wavelengths less than 5.5 μm. For the $8 \div 12$ μm, i.e. for long-wavelength IR band, the PACE-2 has been developed with detectors fabricated on GaAs substrates [8,25÷27]. Because GaAs has a thermal expansion coefficient comparable to CdTe, these PACE-2 FPAs will have the same size limitations as CdTe-based hybrids unless GaAs readout circuits are used. More recently, several laboratories [28÷30] have started manufacturing HgCdTe detector arrays on silicon substrates with the same thermal expansion coefficient as the silicon readout circuit (in the Rockwell International Science Center – PACE-3 process). In the latter process, the thin buffer layer of GaAs on silicon overcomes the nucleation and antiphase domain problems encountered when HgCdTe is grown directly on silicon. Large PACE-3640 × 480 FPAs have been demonstrated [24].

3. Photoemissive detectors

In 1973, Shephered and Yang of Rome Air Development Center proposed the concept of silicide Schottky-barrier detector FPAs as much more reproducible alternative to HgCdTe FPAs for infrared thermal imaging [31]. For the first time it became possible to have much more sophisticated readout schemes – both the detection and the readout could be implemented in one silicon chip. Since then, the development of the Schottky-barrier technology progressed continuously and currently it offers the largest formats of IR image sensors. The important advantage of the Schottky-barrier IR image sensor is the monolithic construction with standard LSI processing. Such attributes as: monolithic construction, uniform responsivity and signal to noise ratio (the performance of an infrared system ultimately depends on the ability to compensate the nonuniformity of an FPA using external electronics and a variety of temperature references), and absence of discernible $1/f$ noise; make Schottky-barrier devices a formidable contender to the main-stream infrared systems and applications.

The most popular Schottky-barrier detector is the PtSi one. It can be used for the detection in the $3 \div 5$ μm spectral range (see Fig. 5). Radiation is transmitted through the p-type silicon and is absorbed in the metal PtSi (not in the semiconductor), producing hot holes which are then emitted over the potential barrier into the silicon, leaving the silicide charged negatively. This fundamental difference in detection mechanism underlies the unique properties of Schottky sensors, including their exceptional spatial unformity and their modified Fowler spectral response. Negative charge of silicide is transferred to a CCD by the direct charge injection method.

The photoyield (electrons/photons) for the process is given by the modified Fowler equation as [23]:

$$Y = \frac{1.24 C_1 (1 - \lambda/\lambda_c)^2}{\lambda} \quad (1)$$

where the cut-off wavelength λ_c in μm is 1.24 Φ_{ms} and Φ_{ms} is the barrier height. C_l is an emission coefficient that depends on the physical and geometrical parameters of the Schottky electrode. Values of λ_c and C_1 as high as 6 μm and 0.5 eV^{-1}, respectively, have been obtained in PtSi [33]. Schottky photoemission is independent on such factors as semiconductor doping, minority carrier lifetime and alloy composition, and as a result of this, it has spatially uniform characteristics which are far superior to those of other detector technologies. Uniformity is only limited by the geometric definition of the detectors. The effective quantum efficiency in the $3 \div 5$ μm atmospheric window is very low, being of order 1%, but using near full-frame integration in array area a satisfactory sensitivity is obtained.

The fundamental source of dark current in the devices is thermionic emission of holes over the potential barrier. Its magnitude is given by Richardson's equation [34]:

$$I_D = A^{**} T^2 \exp\left(-\frac{q\Phi_b}{kT}\right)\left[\exp\left(\frac{q\Phi_b}{kT}\right) - 1\right] \quad (2)$$

where A^{**} is the effective Richardson constant. For holes in silicon, A^{**} is about 30 A/cm^2K^2 in a moderate electric field range [34]. Under reverse biased condition (in infrared image arrays), the barrier is lowered due to the Schottky effect and for reverse bias greater than $3kT/q$ *is:*

$$I_D = A^{**} T^2 \exp\left[-\frac{q(\Phi_b - \Delta\Phi_b)}{kT}\right] \quad (3)$$

where $\Delta\Phi_b$ is the magnitude of the barrier lowering. Fig. 1 shows a very simplified estimate of T_{BLIP} for these devices as a function of cutoff wavelength. The background limited current in 30° FOV is obtained from photoyield equation and Planck's blackbody function. We can see that the cooling requirements are comparable to the extrinsic devices and while an extension of the technology to the long wavelength band is possible using IrSi this will require cooling below 77 K.

The progress of the Schottky-barrier FPA technology has been constant (see Table 2). As Shepherd [38] pointed out, the array size of the Schottky-barrier area FPA has been doubled every 18 months, which is the same as the development rate of the MOS DRAM. The first Schottky-barrier FPA was the 25 × 50 element IR-CCD developed at RCA laboratories under contract for the Rome Air Development Center [39]. The responsivity of this device was very low because a thick PtSi film was used. The quantum efficiency has been improved by

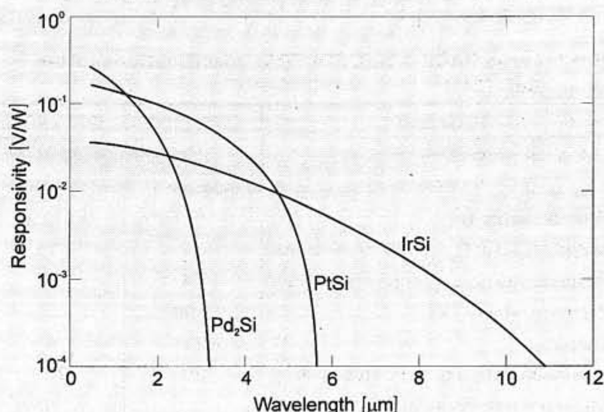

Fig. 5. Spectral response of Pd_2Si, PtSi, and IrSi Schottky-barrier detectors (after Ref. [36])

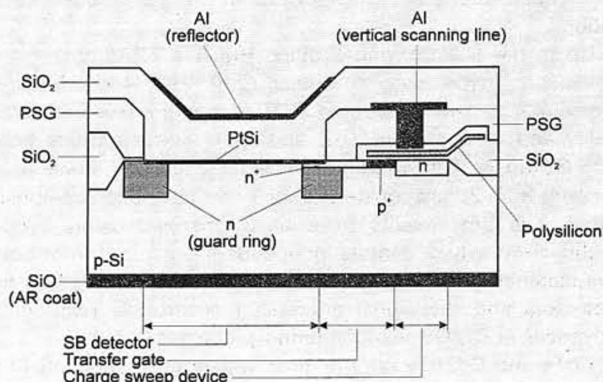

Fig. 6. Pixel cross section of PtSi Schottky-barrier infrared image sensor with CSD readout architecture (after Ref. [36])

Table 2. **Development of PtSi Schottky-barrier FPAs (after Refs. [36] and [37]**

Array size	Type	Pixel size [μm]^2	Year	Fill factor [%]	Company
25 × 25	IL-CCD	160 × 80	1978	17	Sarnoff/RADC
32 × 64	IL-CCD	160 × 80	1981	25	Sarnoff
64 × 128	IL-CCD	133 × 60	1983	22	Sarnoff
64 × 64	IL-CCD	130 × 70	1983	23	Fujitsu
256 × 256	IL-CCD	37 × 31	1983	25	Mitsubishi
160 × 244	IL-CCD	80 × 40	1984	39	Sarnoff
128 × 128	IL-CCD	56 × 42	1985	20	NEC
100 × 100	MOS	50 × 50	1987	66	Mitsubishi
512 × 512	CSD	26 × 20	1987	39	Mitsubishi
160 × 244	IL-CCD	80 × 40	1984	39	Sarnoff
320 × 244	IL-CCD	40 × 40	1988	43	Sarnoff
256 × 256	HB/DRO	30 × 30	1987	85	Hughes
324 × 487	IL-CCD	42 × 21	1988	42	NEC
256 × 244	IL-CCD	31 × 25	1989	36	Loral Fairchild
512 × 512	LACA	32 × 25	1989	36	RADC
640 × 486	IL-CCD	40 × 40	1990	52	Ford
400 × 244	HB/DRO	24 × 24	1990	84	Hughes
640 × 480	MOS	24 × 24	1991	38	Sarnoff
128 × 128	DSI	50 × 50	1990	100	Sarnoff
640 × 488	IL-CCD	21 × 21	1991	40	NEC
640 × 480	HB/DRO	20 × 20	1991	80	Hughes
256 × 256	CSD	52 × 40	1991	66	Mitsubishi
1040 × 1040	CSD	17 × 17	1991	53	Mitsubishi
512 × 512	CSD	26 × 20	1992	71	Mitsubishi
320 × 244	HB/CCD	24 × 24	1992	84	Hughes

IL-CCD: Interline Transfer CCD
CDS: Charge Sweep Device
LACA: Line-Addressed Charge-Accumulation
HB: Hybrid
DRO: Direct Readout
DSI: Direct Schottky Injection

thinning PtSi film. The thinning is effective down to the PtSi thickness of 2 nm [38]. Another way of improving responsivity is implementation of an optical cavity structure, as illustrated in Fig. 6 for the 1040 × 1040 element image sensor [40]. This array has the smallest pixel size (17 × 17 μm^2) among two-dimensional IR FPAs. The pixel was designed with a minimum feature size of 1.5 μm, and the fill factor is 53%.

The responsivity of the image sensors is proportional to their fill factor (the ratio of detector area to the pixel size). Improvement in this factor has been one of the most important in the development of the Schottky-barrier IR image sensor. The technologies developed for this purpose cover the readout architecture, array structure and detector structure. The interline transfer CCD (IL-CCD) architecture is widely used for solid-state imagers. However, it is very difficult to design a small pixel with a large fill factor using this architecture, because the balance between the charge handling capacity of the vertical CCD and the charge storage capacity of the detector has to be considered to obtain the best performance. The typical fill factor of the IL-CCD is 20÷30%. In 1987, the first PtSi Schottky-barrier IR image sensor with full TV resolution was developed using charge sweep device (CSD) readout architecture [41]. The CSD readout architecture is very attractive because this enables enlarging the fill factor without reducing the saturation level of the image sensor. Recently, Kimata et al. [40] have even successfully developed the highest resolution IR image sensor, using the CSD readout architecture. In this device, 1040 × 1040 pixels are integrated on a single chip, and small value of noise equivalent temperature difference of 0.1 K has been achieved with *f*/1.2 optics.

It should be noticed that recent development in the MBE technology made it possible to manufacture high quality Ge_xSi_{1-x} (GeSi) thin films onto silicon substrates. Several works concerning the application of the internal photoemission of GeSi/Si heterojunction diodes for infrared detection have been reported [42÷47]. Lin et al. presented the first GeSi/Si heterojunction detector in 1990 [42, 43]. Photoresponse at wavelength ranging from 2 to 12 μm has been obtained with quantum efficiency 3÷5%. The tailorable cutoff wavelength of these heterojunction detectors has been demonstrated by varying the Ge composition ratio in SiGe layers.

Recently, a 400 × 400 element GeSi/Si heterojunction array with a CCD readout has been developed by Tsaur et al. [46, 47]. They exhibited uncorrected thermal imagers operated at 53 K with cutoff wavelength at 9.3 μm and with minimum resolvable temperature difference of 0.2 K (*f*/2.35). The nonuniformity of resposivity of this array was less than 1%. Although these detectors are in early stage of development, they already outperform IrSi detectors with the same cutoff wavelength with respect to quantum efficiency. It may be possible to increase their quantum efficiency by increasing the absorptance and internal photoemission efficiency by combining optimum SiGe thickness with a cavity structure as it is usually done in PtSi Schottky-barrier detectors.

4. Intersubband GaAs/AlGaAs QWIR detectors

Since the initial proposal by Esaki and Tsu [48] and advent of MBE, the interest in semiconductor superlattice (SL) and quantum well (QW) structures has increased continuously over the years. It has been driven by technological challenges, new physical concepts and phenomena as well as by promising applications. A distinguished feature of these devices is that they can be implemented in chemically stable wide band gap materials as a result of intraband processes. On account of this it is possible to use such material systems as GaAs/AlGaAs, InGaAs/InAlAs, InAs/GaInSb, SiGe/Si, and other systems. Quantum well IR detectors with response in wavelength region from 3 μm to 19 μm have been demonstrated [49, 50].

Between different types of quantum well infrared photodetectors, technology of GaAs/AlGaAs multiquantum well detectors is the most matured. Rapid progress has recently been made in the performance of these detectors [51÷57]. Detectivities have been improved dramatically an they are now high enough so that large 128 × 128 focal plane arrays (FPA's) with long wavelength infrared imaging performance comparable to state of art HgCdTe are produced [58, 59]. With respect to HgCdTe detectors, GaAs/AlGaAs quantum well devices have a number of potential advantages including the use of standard manufacturing techniques based on mature GaAs growth and processing technologies (monolithic integration of these detectors with GaAs FET's, charge coupled devices and high-speed signal processing electronics is possible), highly uniform and well controlled MBE growth on over 3-inch GaAs wafers, high yield and thus low cost, more thermal stability and intrinsic radiation hardness.

Kinch and Yariv [60] have presented an investigation of the fundamental physical limitations of individual GaAs/AlGaAs multiple quantum well infrared detectors as compared to ideal HgCdTe photoconductors with cut-off wavelengths λ_c = 8.3 μm and 10 μm. It appears, that in temperature range 40÷100 K the thermal generation rate is approximately five orders of magnitude smaller than in the corresponding GaAs/AlGaAs superlattice. The dominant factor favoring HgCdTe in this comparison is the lifetime of excess carriers, which for *n*-type HgCdTe is above 10^{-6} s at 80 K, compared to about 10^{-11} s for the GaAs/AlGaAs superlattice. In the superlattice the confined carriers are free to move within the plane (there is no energy gap separating confined from unconfined states), so the carrier recombination rate is very high.

At present, the HgCdTe photodiodes are preferred over photoconductors due to their very low power dissipation and relatively high impendance matched directly into input stage of a silicon CCD in hybrid two-dimensional FPAs. Despite a great research and development efforts, large photovoltaic HgCdTe FPAs remain expensive, primarily because of the low yield of operable arrays. The low yield is due to the high incidence of electrically active defects and to the sensitivity of LWIR HgCdTe devices to defects and surface leakage, which is a consequence of basic material properties. Competitive GaAs/AlGaAs technology with advantages in uniformity, controllability, and yield is useful for producing large arrays.

It appears that detectivity of GaAs/AlGaAs quantum well infrared photoconductors (QWIP) depends quite weakly on both the doping concentration (in the range 10^{16} to 10^{18} cm^{-3}) and the bias voltage V_b (less than a few volts) [53]. Note, as discussed in detail in Ref. [53], that for a good approximation we have:

$$D^* = D_o^* \exp\left(\frac{hc}{2kT\lambda_c}\right) \quad (4)$$

According to Levine et al. [56, 57] the best fit $T = 77$ K detectivity for the n-type GaAs/AlGaAs QWIPs is

$$D^*[\mathrm{cm\,Hz^{1/2}W^{-1}}] = 1.1 \cdot 10^6 \exp\left(\frac{hc}{2kT\lambda_c}\right) \quad (5)$$

It should be noted that although Eq. (5) fits to data taken at 77 K, this equation is expected to be valid over a wide range of temperature.

The dependence of detectivity on the long wavelength cut-off for QWIPs at different temperatures is shown in Fig. 7. We can see very good agreement between curves calculated according to equation (2) and experimental data in wide wavelength ranges of cut-off wavelength $9\ \mu m \leqslant \lambda_c \leqslant 19\ \mu m$ and temperature $35\ K \leqslant T \leqslant 77$ K. It should be stressed that agreement is satisfying considering the samples have different doping, different methods of crystal growth (MBE, MOCVD, and gas source MBE), different spectral widths, different excited states (continuum, bound, and quasi-continuum) and even in the cse of different materials systems (InGaAs) [56, 57, 61].

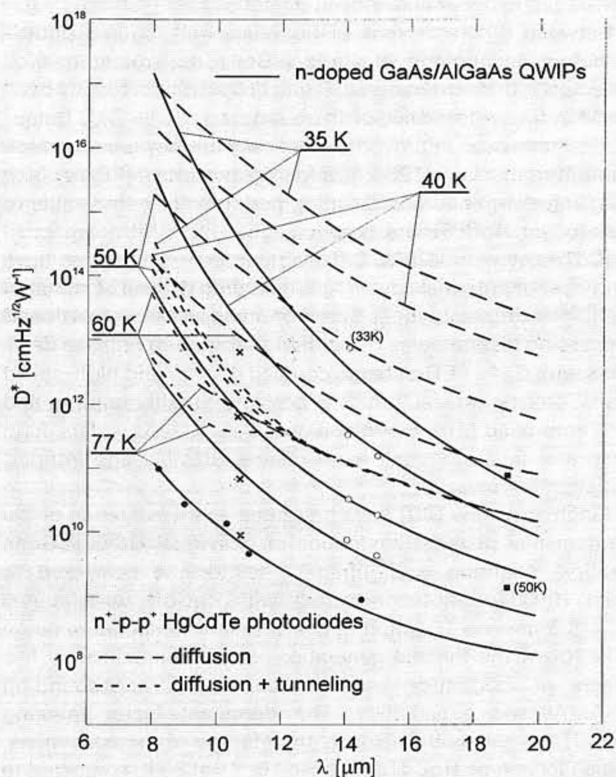

Fig. 7. Dependence of detectivity on the long wavelength cut-off for n-doped GaAs/AlGaAs QWIPs and n^+-p-n^+ HgCdTe photodiodes at temperatures $\leqslant 77$ K. The experimental data for QWIPs are taken from Refs. [53] (×), [54] (○), [55] (■), [56] (●), and [61] (+)

The comparison of detectivity of GaAs/AlGaAs QWIPs with the theoretical ultimate performance of n^+-p-p^+ HgCdTe photodiodes (dashed lines) calculated assuming that R_oA product is limited by diffusion current is also shown in Fig. 7. We can see that for $\lambda_c \approx 8\ \mu m$, the detectivity of both types of detectors is comarable at 40 K, and at lower temperatures QWIPs exhibit an advantage of performance. In the range of longer cut-off wavelength, the detectivity of HgCdTe photodiodes is higher. This advantage of HgCdTe photodiodes increases with increasing of long-wavelength cut-off. Usually however, in temperature range below 50 K the limiting performance of the HgCdTe photodiodes is determined by trap-assisted tunneling [62÷66]. The above comparison of detectivity with included influence of trap-assisted tunneling is more advantageous for GaAs/AlGaAs QWIPs in wide spectral region. It is very important, because in longer wavelength region the compositional uniformity of HgCdTe FPAs is worse.

In the above considerations we compared performance of QWIPs and HgCdTe photodiodes assuming thermal noise-limited detectivity as a criterion of comparison. It means that we considered the performance of these detectors for low background applications. However, it should be noticed that for large FPAs the relevant figure of merit is noise equivalent temperature difference ($NE\Delta T$), i.e. the temperature change of a scene required to produce a signal equal to the rms noise. An array having $D^* = 10^{10}$ $\mathrm{cmHz^{1/2}W^{-1}}$ would achieve a very sensitive $NE\Delta T = 0.01$ K [67]. This would produce an excellent image, comparable or superior to that of present arrays which are uniformity limited. In this regard, it is worth noting even for a highly uniform array having only a 0.1% pixel variation, that this small non-uniformity would limit $NE\Delta T$ to 0.06 K. Thus higher values of detectivity are unnecessary and in fact they will not improve this limit.

The important strengths of GaAs/AlGaAs QWIPs are the highly advanced material systems and their capability to rapidly fabricate devices of new design by programming the MBE system. Recently, Levine et al. [59] have presented thermal imaging data of hybrid 128 × 128 GaAs/AlGaAs FPA consisting of 50 × 50 μm square photoconductors with peak response at $\lambda_p = 9\ \mu m$. The 99% yield of this array technology is a result of the excellent MBE grown uniformity of thickness (1%) and the matured processing technology. After correction, the measured non-uniformity of the array was better than 0.1%, and the $NE\Delta T$ of 0.01 K was observed at 60 K.

For QWIPs detectors to be background limited, they will have to operate at temperatures below 77 K (see Fig. 1). It should be noticed that QWIP FPAs are far from optimum. Improvements which include the use of two-dimensional gratings, cavity design and optimizations of dopants, magnitude and profile could cumulatively result in a fold improvement in responsivity [18, 68] and raise the operation temperature. Then QWIP FPAs with peak responsivity 8÷10 μm, should be operated at temperature 77 K.

Operability of HgCdTe photodiodes at temperatures about 40 K is limited to 70÷80%. Pixel yield and uniformity of FPAs are key issues for low background applications. In this context, GaAs/AlGaAs QWIPs promise high yield due to well established and highly uniform MBE growth and GaAs processing technologies in FPAs. GaAs quantum well detector FPAs are expected to combine the advantages of PtSi Schottky barrier arrays (high uniformity, high yield, radiation hardness, large

arrays with monolithically integrated electronics, low cost) with the advantages of HgCdTe (high quantum efficiency and long wavelength response). QWIP FPAs can found strategic applications, if it is taken into account that at about 40 K in spectral range 8 ÷ 10 μm, the detectivity of QWIPs is comparable to the best HgCdTe photodiodes (and is background limited), and uniformity of quantum well detector arrays is higher.

Further improvements in QWIPs detectors technology could results in improvement of responsivity and raise the operation temperature of FPAs to 77 K in LWIR spectral region.

5. Ways to improve the performance of near room temperature detectors

The present uncooled and near room temperature detectors are sub-BLIP detectors. This makes them inadequate in many applications and it is highly desirable to improve their performance. The ultimate goal is to obrain near-BLIP performance at ambient temperature, or at least at temperatures achievable with thermoelectric coolers.

To discus the possibilities of improving the performance of high temperature photodetectors let us consider a simplified theory of ultimate detectivity based on thermal generation and recombination rates. The model is generally applicable to a wide variety of IR devices. We consider a photoconductor as a slab of semiconductor with an actual electrical area A_e and thickness t.

The current responsivity is determined by quantum efficiency η and by photoelectrical gain g. The photoelectrical gain is the number of carriers passing contacts per one generated pair. Both η and g are assumed to be constant over the active detector area. For monochromatic radiation the responsivity is equal

$$R_i = \frac{\lambda}{hc}\eta q g \tag{6}$$

The signal-to-noise ratio, or detectivity, is usually limited by statistical fluctuations of the thermal generation and recombination rates. It should be noted that the contribution of recombination rate fluctuations to the noise can be avoided sometimes by locating recombination in a region where it has little effect, for example in the neutral regions of a reverse biased photodiode over the contacts of a sweep-out photoconductor.

The noise current is [69]

$$I_n = [2(G+R)A_e t]^{1/2} q g \Delta f \tag{7}$$

and then detectivity characterizing normalized signal-to-noise performance of detector

$$D^* = \frac{R_1 (A_o \Delta f)^{1/2}}{I_n} = \frac{\lambda}{hc}\left(\frac{A_o}{A_e}\right)^{1/2} \frac{\eta}{t^{1/2}} [2(G+R)]^{-1/2} \tag{8}$$

As the latter equation shows, the detectivity at a given wavelength can be maximized if: the ratio of optical area to electrical one is high, the ratio of quantum efficiency to square root of thickness is high, and the sum of generation rate and recombination one is low.

In most detectors $A_o \approx A_e$. There are ways to make the optical area substantially greater than the electrical one. The optical immersion of detectors to a hemispherical or hyperhemispherical lens of high refraction index is an example of very effective way to increase the A_o/A_e ratio [4,70÷72]. Fig. 8 schematically shows the structure of a monolithic, optically immersed HgCdTe photoconductor. Optical immersion offers the additional advantage of reducing bias power dissipation by factor of n^2 and n^4 in the case of hemi-and hyperhemisherical immersion, respectively. As Fig. 9 shows, the performance of immersed devices has been highly improved comparing to that of conventional, non-immersed devices operating under the same conditions. Optical immersion can also be used successfully for photoelectromagnetic, Dember effect and photodiode detectors [4].

Since the detectivity is proportional to the factor $\eta/t^{1/2}$, a high quantum efficiency must be achieved in thin devices. This is usually difficult to make, as the absorption of long wavelength radiation in uncooled, narrow-gap semiconductors is weak. The quantum efficiency can be increased in devices with non-reflective frontside and highly reflective backside surfaces of the sensitive element. The effective absorption can be further improved by using the interference effect [4, 73] to setup the resonant cavity.

As equation (6) shows, the generation and recombination rates should be minimized. At high temperature the thermal generation and recombination in HgCdTe and in other narrow-gap semiconductors with InSb-like band structure is determined by the Auger-1 and Auger-7 processes. The corresponding net generation rate (the difference between the generation and recombination rates) is [74]

$$G_A - R_A = \frac{n_i^2 - np}{2n_i^2}\left[\frac{n}{(1+\alpha n)\tau_{A1}^i} + \frac{p}{\tau_{A7}^i}\right] \tag{9}$$

where τ_{Ai}^i and τ_{A7}^i are the intrinsic Auger-1 and Auger-7 recombination times, n_i is the intrinsic carrier concentration and $\alpha^{-1} = 1.9 \times 10^{17}$ cm^{-3}. As equation shows, in the equilibrium state, the net Auger generation and recombination rates are

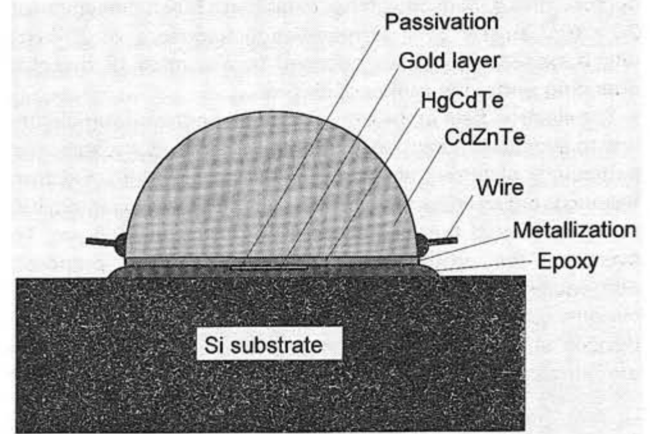

Fig. 8. Structute of monolithic optically immersed HgCdTe photoconductor (after Ref. [70])

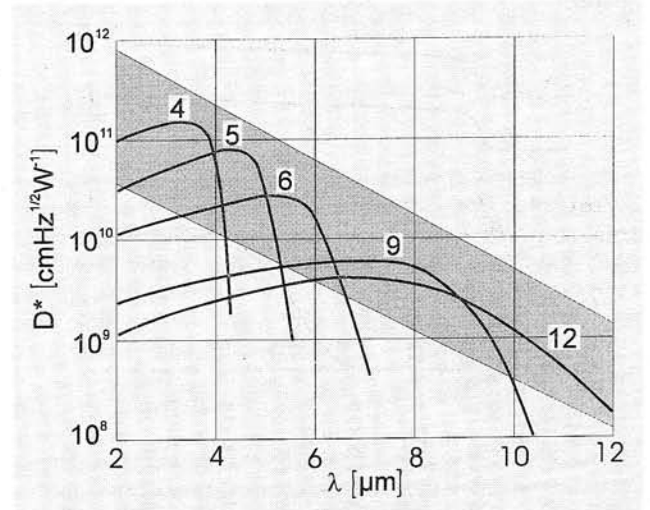

Fig. 9. Typical spectral detectivity of optically immersed termoelectrically cooled PCI-2TE HgCdTe photoconductors (after VIGO Data Sheets, Warsaw 1993)

equal. Both rates increase exponentially with temperature. Since τ_{A1}^{i} is by a factor of 2 to 10 shorter than τ_{A7}^{i}, the G_A+R_A achieves its minimum in lightly doped p-type material. This is the reason why p-type doping is preferable for equilibrium mode detectors operated at high temperature.

Elliott and other British scientists [75÷78] have proposed a new approach to reduce the detector cooling requirements, which is based on the non-equilibrium mode of operation. Their concept relies on the suppression of the Auger processes by decreasing the free carrier concentration below its equilibrium values. This can be achieved, for example, in a biased *l-h* or heterojunction contacts.

An example of excluding contact photoconductor material is shown in Fig. 10. The positively biased contact is a highly doped n^+ or wide-gap material, while the photosensitive area is a near-intrinsic n-type (ν) material. Such a contact does not inject minority holes but permits the majority electrons to flow out of the device. As a result, the hole concentration also falls, to maintain electrical neutrality in the region. Reduced concentration of electrons and holes result in the suppression of the Auger processes. The devices have been prepared for low concentration n-type bulk HgCdTe, with the n^+ regions formed by ion milling. A large increase in reverse bias responsivity has been observed comparing to that at the same direct current. The improvement in the detectivity was more modest owing to high flicker noise at reverse bias. An uncooled 10×10 μm photoconductor with a 4.2 μm cut-off has exhibited a 500 K detectivity of 2.7×10^{10} cmHz$^{1/2}$W^{-1} at modulation frequency of 20 kHz, which exceeds the values obtained by any other IR detector operating under the same conditions.

The electron field in the excluded region must be sufficiently low to avoid significant heating in the devices as a whole, and particularly electrons above the lattice temperature. Electron heating is not an important constraint in the 3÷5 μm region, but seems to restrict the usefulness of exclusion at 10.6 μm. To overcome the problem, the same British team proposed non-equilibrium photodiode structures, which employ both minority carrier exclusion and extraction [75÷81]. These devices, shown in Fig. 11, consist of three layers. The first is a wide-gap n or n^+, the second is narrow-gap and lightly doped π-type, and the third is a wide-gap p or p^+. When the diode is reverse biased, the junction between π and n-type extracts electrons, which cannot be replenished by the excluding p^+-π contact so the electron density drops by several orders of magnitude throughout the π region. The hole concentration also falls to keep space charge neutrality. It results in suppression of Auger processes and in noise reduction.

Another method to obtain stationary non-equilibrium depletion of the semiconductor is using the magnetoconcentration effect [82,83]. The depletion in the device is achieved due to the Lorentz force which deflects both the electron and the hole towards the backside surface of the high surface recombination. As a result, most of the semiconductor becomes highly depleted.

The BLIP limit can be achieved using materials of extremely high quality, with controlled doping at very low levels ($<10^{13}$ cm^{-3}) and with a very low concentration of Schockley-Read centers. The achievement of potential performance of the non-equilibrium device in practice would require well-established epitaxial technology, which is not yet sufficiently developed.

6. Thermal detectors

Present-day IR semiconductor imagers use cryogenic or thermoelectric coolers, complex IR optics, and expensive sensor materials. Typical cost of cryogenically cooled imagers amounts to ca. $100000 (see Table 3), which restrict their installation to critical military applications allowing operation in complete darkness (such as tanks and aircrafts) [84].

However, the longer term picture could be changed dramatically as a result of current research activities in low-cost uncooled imaging systems manufactured with thermal detectors. Thermal detectors have been rarely used in scanned imagers because of their slow response. They are currently of considerable interest for two-dimensional electronically addressed arrays, where the bandwidth is low and the ability of thermal devices to integrate for a frame time is an advantage. It results from Fig. 4 that the thermal detector which are relative newcomers are narrowing the gap with photon detectors.

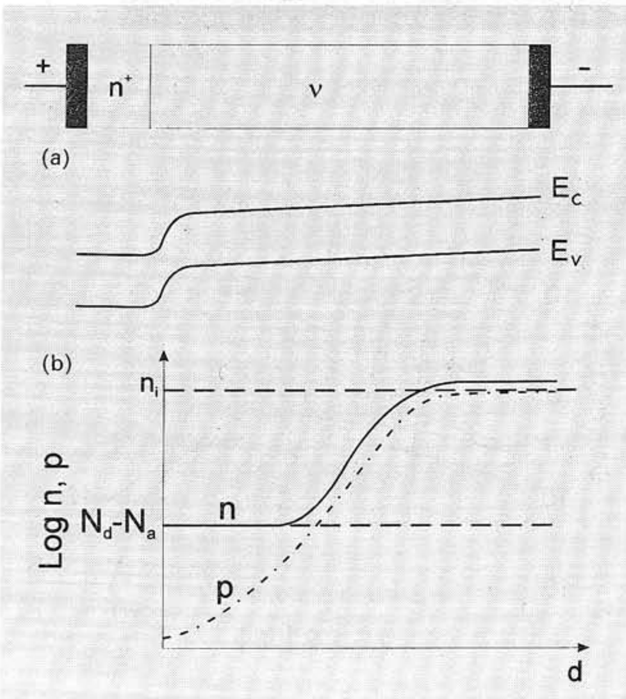

Fig. 10. Schematic structure of excluded contact photoconductor (a) and energy levels diagram (b) (after Ref. [76])

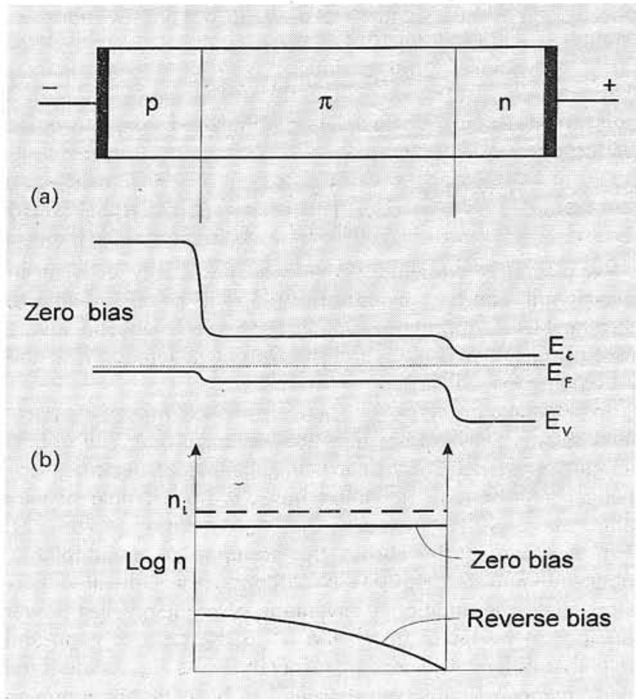

Fig. 11. Schematic structure of extracted photodiode, showing energy levels (a) and electron concentration (b) (after Ref. [76])

Table 3. **Comparison of IR imagers (after Ref. [84])**

Feature	Present scanned cryogenic imagers	Cryogenic staring imagers	Uncooled silicon microbolometer imagers
Approximate system cost	$ 100 000 (military volume production)	$ 100 000 (military volume production)	$ 1000 (high-volume production)
Typical focal-plane temperature	100 K	100 K	Room temperature
IR sensor	HgCdTe, InSb	HgCdTe, InSb, PtSi, GaAs/AlGaAs	Micromachined silicon
Typical *NEΔT*	0.1°C	0.1°C	0.05°C
Applications	Military and specialized industrial applications	Military and specjalized industrial applications	Widespread applications for military, commerce, research, industry, etc.

In the case of thermal detectors the radiation is absorbed to change the temperature of the material and the resultant change of some physical properties is used to generate an electrical output. The fundamental limit of the sensitivity of this process is given by the "effective conductivity" G_T of the radiation process which connects the detector to outside world. This limit (when the detector is thermally isolated so that energy interchanges with the surroundings only by radiation exchanged over the whole hemisphere above an absorbing face) is given by

$$G_T = 4\sigma T^3 \tag{10}$$

where σ is Stefan's constant. The detector will experience a fluctuation spectrum with an rms value [85]

$$P_T = (4kT^2 G_T A)^{1/2} \tag{11}$$

The temperature noise voltage is calculated by treating P_T in the same way as an incoming signal. Hence

$$V_n = R_v (4kT^2 G_T A \Delta f)^{1/2} \tag{12}$$

where R_v is the voltage responsivity. This gives the background limit to detectivity

$$D^* = \frac{R_v (A\Delta f)^{1/2}}{V_n} = \frac{1}{2T(kG_T)^{1/2}} \tag{13}$$

which for ideal thermal detector is equal $(16k\sigma T^5)^{-1/2} = 1.8 \cdot 10^{10}$ cmHz$^{1/2}$W^{-1}.

In practice, the performance of the array is limited by other factors. One of them is the thermal admittance Y of the detector element

$$|Y|^2 = G^2 + \omega^2 C^2 \tag{14}$$

where G is the thermal conductance and C is the thermal capacitance of the detector. The value of G is determined by the isolation of the detector from its surroundings. The main factors affecting this are the method of supporting the detectors and the electrical interconnections which also conduct heat. Modern technology enables a value of thermal conductance between the device and its heat sink of 0.5 Wcm^{-2}K^{-1} which would limit the detectivity to about $7 \cdot 10^8$ cmHz$^{1/2}$W^{-1}. This is about a factor of 20 below the theoretical limit. Other factors that affect the array performance are primarily due to noise in the readout circuits and the noise due to losses in the detector. These sources of noise do not dominate in present detectors [86,87]. However, if the thermal conductance of the detector is reduced, resulting in lower detector noise V_n, see Eq. (12), these sources of noise would dominate.

6.1. Pyroelectric detectors

The pyroelectric detectors employs the temperature dependent internal polarization of a ferroelectric material. Several successful commercial products have been produced. The best examples of these are the application of single element ceramic detectors in intruder alarms and the use of the pyroelectric vidicons with a triglycine sulphate target in the fire service cameras.

In order to combine detectors into large two-dimensional arrays, the detectors must be buffered with a preamplifier and multiplexed to a single output. The IR radiation focused onto the array is modulated by a chopper. The chopped radiation produces alternative warming and cooling of the array and this results in alternate positive and negative signals. The array output is stored in a field store and the alternate positive and negative fields are subtracted in a image difference processor. Spurious fixed pattern noise on the outputs is removed during this operation.

In order to obtain TV-rate thermal imagers using pyroelectrics, a special solder bump hybridization procedure ensured low thermal conductance between pyroelectric detectors (made from modified zirconate target) and silicon addressing circuity has been developed (see Fig. 12). A ceramic ferroelectric detector element is connected by a solder bump, which is much smaller than the detector element to minimize the thermal conductance, to a contact pad on a silicon circuit. This type of interconnect can give a thermal conductance to the substrate in the region of 50 μW/K. Fig. 12 also shows the separation of individual elements by reticulation grooves to reduce the lateral

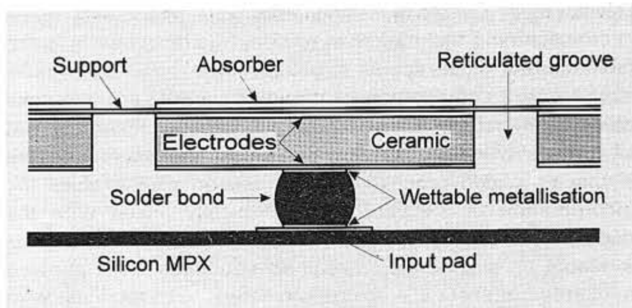

Fig. 12. Schematic of a possible structure for a thermal detector hybrid array (after Ref. [88])

diffusion of heat to adjacent elements, what improve thermal resolution at high spatial frequencies. Recent work has shown that it is possible to reticulate pyroelectric targets by using either ion-beam milling or laser induced chemical etching [87]. Devices with 100 μm pitch and up to 100×100 elements have been produced, with *NEΔT* of better than 0.5 K and potentially 0.1 K seems to be achievable [88].

6.2. Bolometers

Another possible way of achieving an array of thermal detectors is using the change of resistance of a material with temperature. This can be done with a wide variety of materials to produce an array of bolometers. Just a few works have been reported on arrays of these devices. If a material is suitable for silicon technology then it will be very attractive.

The fact remains that NEΔT for any of array configurations may be expressed [89]

$$NE\Delta T = \frac{4F^2(\Delta f^2)^{1/2}}{A^{1/2} t N^{1/2} M^*} \tag{15}$$

where F is the f-number of the optics, t is the transmission of the optics, Δf is the electrical bandwidth of the system, $N = n \times m$ the number of detectors in the array and M^* is the normalized thermal figure of merit which describes the detector's ability to detect thermal radiation. It is related for the more familiar figure of merit D^* by

$$M^* = \int_\lambda D^*(\lambda) A(L, \lambda) \left.\frac{\partial e(\lambda, T)}{\partial T}\right|_{T_t} d\lambda \tag{16}$$

where $A(L, \lambda)$ is the atmospheric transmittance and $e(\lambda, T)$ is the spectral radiant emittance of a blackbody target of temperature T_t at range L. For thermal detector in ideal conditions ($A=1$) is $M^* = 4\sigma T^3 D^*$.

Let us calculate $NE\Delta T$ for a single thermal detector. We assume the size of active element 0.1×0.1 mm^2, detectivity $10^8 \div 10^9$ cmHz$^{1/2}$W^{-1}, transmission of optics $t=1$ and $F=1$. In the case of non-scanned array, when each element sees all the time the very same pixel on target, indispensable bandwidth is low. Assuming that response time is $\tau = 1/60$ s, the electrical bandwidth is $\Delta f = (2\pi\tau)^{-1} = 10$ Hz. Then, it results from equation (15) the possibility of achieving $NE\Delta T$ between 2 and 20 mK, depending on assumed detectivity D^*! Hence, the thermal detector array can resolve very small temperature differences, comparable to those attained with the scanned cryogenic imagers. Analysis of the mechanism that limits the sensitivity of thermal detectors shows that their maximum possible sensitivity is determined by a single factor, i.e. the attainable thermal isolation defined as the thermal resistance between the detector and its surroundings.

In 1979, Honeywell's researchers at the Sensor and System Development Center in Minneapolis were developing novel micromachining techniques in silicon. Micromachining is the fabrication of small, robust structures, with submicron precision, using a combination of photolithography and selective etching. Micromachining is possible in many materials, but silicon is favored because many micromachining techniques are similar to silicon-processing ones. Silicon also enables the incorporation of electronics monolithically linked with the microstructures. An extremely high thermal resistance was available in silicon micromachined structures. This allowed miniature bolometers — microbolometers — to fabricate with thermal isolation close to the attainable physical limit which is about 10^8 °C/W for a 50 μm square detector. It was demonstrated that, with a microbolometer having a thermal isolation of 10^7 °C/W, a typical incident IR signal of 10 nW was sufficient to change the microbolometer temperature by 0.1°C.

At present, a new revolution in reducing cost of thermal imagers, which is now underway, is caused by very encouraging results obtained with micromachined silicon bolometer arrays. A typical microbolometer design consists of a 0.5 μm thick plate suspended clear of the underlying silicon by two "legs" that provide the required high thermal resistance between the suspended plate and its surroundings, allowing the plate to respond to incident IR radiation. The temperature changes in the suspended plate are sensed by circuitry, which is monolithically integrated into underlying silicon and connected to the suspended plate by thin-film metallizations on the legs. The 240 × 336 arrays of 50 μm microbolometers are fabricated complete with monolithic readout circuits integrated into underlying silicon. An average $NE\Delta T$ of better than 0.05 K was demonstrated with a Honneywell uncooled imager fitted with an $f/1$ optics (see Fig. 13) [84]. This sensitivity is better than

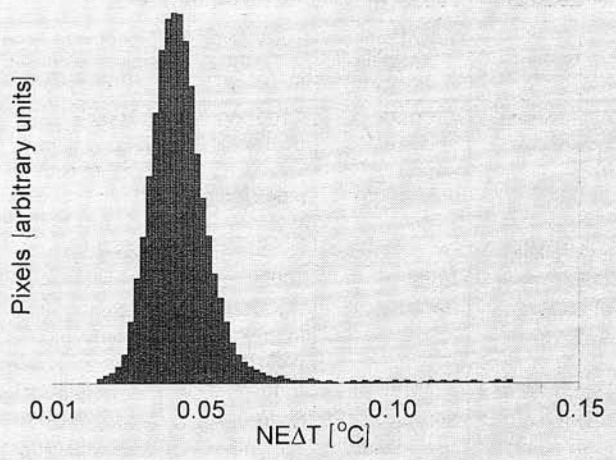

Fig. 13. Histogram of measured $NE\Delta T$ of microbolometers in 240 × 336 uncooled array shows mean $NE\Delta T$ of less than 0.05 °C with a $f/1$ optics (dead pixels are not included) (after Ref. [84])

that attained with scanned cryogenic imagers currently used in military applications. Uncooled, monolithic FPAs of silicon may revolutionize development of thermal imagers. It is expected that high-performance imager system cost will be reduced by about two orders of magnitude, to less than 1000, and the above mentioned IR cameras will become widely available in the next decade. Although developed for military applications, low-cost IR imagers will likely be used in nonmilitary areas such as: drivers aid, aircraft aid, industrial process monitoring, civil services, etc.

7. Conclusions

At present, it is really difficult to foresee the future development of IR detectors. In 1974 Harman and Melngailis wrote [90]: *In comparing the two materials* ($Hg_{1-x}Cd_xTe$ *and* $Pb_{1-x}Sn_xTe$) *we anticipate that* $Pb_{1-x}Sn_xTe$ *will be more widely used in the future for detection of blackbody radiation in 8÷14 μm region because crystal growth techniques for this alloy are potentially cheaper and adaptable to mass production. In addition,* $Pb_{1-x}Sn_xTe$ *appears to be more stable and less likely to degrade at elevated temperature than* $Hg_{1-x}Cd_xTe$. Four years later [91] it was clear that due to two drawbacks of IV–VI compounds (high dielectric constant and high thermal coefficient of expansion), HgCdTe won this competition.

In the near term HgCdTe alloy seems to be unchallenged as the most important material for high performance and fast single element and small array IR detectors. The same seems to be true in applications for thermal imagers of highest performance. Schottky-barrier arrays are likely to take over increasingly applications requiring high spatial resolution for which the 3÷5 μm band is acceptable. GaAs/AlGaAs QWIP arrays are predicted for low background long-wavelength space applications. Thermal detectors are poised to take over and increase the market for uncooled short range imaging systems.

The long term picture however could change dramatically as a result of current research activities. Thermal detector arrays will increase in size and improve in thermal sensitivity to a level satisfying high performance applications at ambient temperature. In the next decade, low-cost IR thermal imagers (both pyroelectric devices and bolometers) will be used likely in non-military applications such as: drivers aid, aircraft aid, industrial process monitoring, community services, etc. The low temperature growth of HgCdTe on alternative substrates containing silicon circuits may render Schottky barrier devices with their fundamental physical limitations and stringent cooling

requirements. The narrow gap intrinsic semiconductors, possibly those operated in non-equilibrium mode, are likely to be unchallenged for high detectivity and fast single element and small array IR systems. The situation concerning quantum well structures and superlattices is not clear. However, unique detection capabilities may arise from the low dimensional solids.

References

1. *C.T. Elliott:* Proc. SPIE, **915** (1988) p. 9.
2. *C.T. Elliott*: in: Handbook of Semiconductors (*C. Hilsum* – ed.). North Holland, Amsterdam 1982, vol. 4, p. 727.
3. *A. Rogalski, J. Piotrowski:* Prog. Quantum. Electron., **12** (1988) p. 87.
4. *J. Piotrowski, W. Galus, J. Piotrowski:* Infrared Phys., **31** (1991) p. 1.
5. *N. Bluzer, A.S. Jensen:* Opt. Eng., **26** (1987) p. 241.
6. *A. Rogalski, W. Larkowski:* Electron Technol., **18** (1985) p. 55.
7. *J.M. Arias* et al.: J. Appl. Phys., **65** (1989) p. 1747.
8. *L.O. Bubulac* et al.: Semicond. Sci. Technol., **5** (1990) p. S45.
9. *J.M. Arias* et al.: J. Appl. Phys., **69** (1991) p. 2143.
10. *G.N. Pultz* et al.: J. Vac. Sci. Technol. B, **9** (1991) p. 1724.
11. *C.C. Wang:* ibid. [10] p. 1740.
12. *J.M. Arias* et al.: Appl. Phys. Lett., **62** (1993) p. 976.
13. *Y. Nemirovsky, G. Bahir:* J. Vac. Sci. Technol. A, **7** (1989) p. 450.
14. *W.E. Tennant* et al.: J. Vac. Sci. Technol. B, **10** (1989) p. 1359.
15. *A. Rogalski* et al.: Infrared Phys., **33** (1992) p. 463.
16. *M. Kurata:* Numerical Analysis of Semiconductor Devices. Lexington Books, Lexington 1982.
17. *P.R. Norton:* Opt. Eng., **30** (1991) p. 1649.
18. *R.E. DeWames* et al.: Proc. SPIE, **1735** (1993) (in print).
19. *R.E. DeWames* et al.: J. Cryst. Growth, **86** (1988) p. 849.
20. *R.E. DeWames* et al.: J. Vac. Sci. Technol. A, **6** (1988) p. 2655.
21. *E.R. Gertner* et al.: J. Cryst. Growth, **72** (1985) p. 462.
22. *L.O. Bubulac:* ibid. [21], p. 478.
23. *R.B. Bailey* et al.: IEEE Trans. Electron Devices, **ED-38** (1991) p. 1104.
24. *L.J. Kozlowski* et al.: Proc. SPIE, **1540** (1991) p. 250.
25. *D.D. Edwall, E.R. Gertner, L.O. Bubulac:* J. Cryst. Growth, **86** (1988) p. 240.
26. *D.D. Edwall* et al.: Semicond. Sci. Technol., **5** (1990) p. 221.
27. *L.M. Smith* et al.: J. Cryst. Growth, **107** (1991) p. 605.
28. *R. Kay* et al.: Appl. Phys. Lett., **51** (1987) p. 2211.
29. *S.M. Johnson* et al.: Appl. Phys. Lett., **56** (1990) p. 946.
30. *K. Zanio:* ibid. [29], p. 946.
31. *F.D. Shepherd, A.C. Yang:* Tech. Digest of IEDM, **310** (1973).
32. *W.F. Kosonocky:* Proc. SPIE, **869** (1987) p. 90.
33. *F.D. Shepherd:* Proc. SPIE, **443** (1984) p. 42.
34. *S.M. Sze:* Physics of Semiconductor Devices. J. Wiley & Sons, New York 1982.
35. *F.D. Shepherd:* Proc. SPIE, **930** (1988) p. 2.
36. *M. Kimata, N. Tsubouchi*: in: Semiconductor Infrared Detectors. (*A. Rogalski* – ed.). SPIE Optical Engineering Press, will be published.
37. *W.F. Kosonocky:* Proc. SPIE, **1308** (1990) p. 2.
38. *F.D. Shepherd:* Tech. Digest IEDM, **370** (1984).
39. *E.S. Kohn, W.F. Kosonocky, F.V. Shallcross:* Final Report RADC-TR-308, Rome Air Development Center 1977.
40. *M. Kimata, N. Yutani, N. Tsubouchi:* Proc. SPIE, **1656** (1992) p. 151.
41. *M. Kimata* et al.: IEEE J. Solid-State Circuits, **SC-22** (1987) p. 1124.
42. *T.L. Lin, J. Maserjia:* Appl. Phys. Lett., **57** (1990) p. 1422.
43. *T.L. Lin* et al.: Tech. Digest of IEDM, **641** (1990).
44. *T.L. Lin* et al.: IEEE Trans. Electron Devices, **ED-38** (1991) p. 1141.
45. *T.L. Lin* et al.: Proc. SPIE, **1540** (1991) p. 135.
46. *B.Y. Tsaur, C.K. Chen, S.A. Marino:* IEEE Electron Device Lett., **12** (1991) p. 293.
47. *B.Y. Tsaur, C.K. Chen, S.A. Marino:* Proc. SPIE, **1540** (1991) p. 580.
48. *L. Esaki, R. Tsu:* IBM J. Res. Develop., **14** (1970) p. 61.
49. *F.F. Sizov, A. Rogalski:* Prog. Quantum Electron., **17** (1993) p. 93.
50. *F.F. Sizov, A. Rogalski:* Opto-Electronics Review, no. 1 (1993) p. 3.
51. *B.F. Levine* et al.: Appl. Phys. Lett., **53** (1988) p. 2196.
52. *B.F. Levine* et al.: Appl. Phys. Lett., **56** (1990) p. 851.
53. *S.D. Gunapala* et al.: J. Appl. Phys., **69** (1991) p. 6517.
54. *A. Zussman* et al.: J. Appl. Phys., **70** (1991) p. 5101.
55. *B.F. Levine* et al.: J. Appl. Phys., **71** (1992) p. 5130.
56. *B.F. Levine* et al.: J. Appl. Phys., **72** (1992) p. 4429.
57. *B.F. Levine:* Semicond. Sci. Technol., **8** (1993) p. S400.
58. *L.J. Kozlowski* et al.: IEEE Trans. Electron Devices, **ED-38** (1991) p. 1124.
59. *B.F. Levine* et al.: Semicond. Sci. Technol., **6** (1991) p. C114.
60. *M.A. Kinch, A. Yariv:* Appl. Phys. Lett., **55** (1989) p. 2093.
61. *S.D. Gunapala* et al.: Appl Phys. Lett., **58** (1991) p. 2024.
62. *I. Wong:* IEEE Trans. Electron Devices, **ED-27** (1980) p. 48.
63. *R.E. DeWames* et al.: J. Cryst. Growth, **86** (1988) p. 849.
64. *Y. Nemirovsky* et al.: J. Vac. Sci. Technol. A, **7** (1989) p. 528.
65. *Y. Nemirovsky* et al.: J. Vac. Sci. Technol. B, **9** (1991) p. 1829.
66. *Y. Nemirovsky, A. Unikovsky:* J. Vac. Sci. Technol. B, **10** (1992) p. 1602.
67. *C.G. Bethea* et al.: IEEE Trans. Electron Devices, **ED-38** (1991) p. 1118.
68. *F.W. Adams* et al.: Proc. SPIE, **1541** (1991) p. 24.
69. *A. Rose:* Concepts of Photoconductivity and Allied Problems. Interscience Publishers, New York 1963.
70. *M. Grudzień, J. Piotrowski:* Infrared Phys., **29** (1989) p. 251.
71. *N.T. Gordon:* Semicond. Sci. Technol., **8** (1991) p. 106.
72. *C.L. Jones* et al.: ibid. [71], p. 110.
73. *M. Nowak:* Prog. Quantum Electron., **11** (1987) p. 205.
74. *A.M. White:* Infrared Phys., **25** (1985) p. 729.
75. *T. Ashley, C.T. Elliott:* Electron. Lett., **21** (1985) p. 451.
76. *T. Ashley, C.T. Elliott, A.M. White:* Proc. SPIE, **572** (1985) p. 123.
77. *T. Ashley, C.T. Elliott, A.T. Harker:* Infrared Phys., **26** (1986) p. 303.
78. *C.T. Elliott:* Semicond. Sci. Technol., **5** (1990) p. S30.
79. *T. Ashley* et al.: Proc. SPIE, **1361** (1990) p. 238.
80. *T. Ashlet, C.T. Elliott:* Semicond. Sci. Technol., **6** (1991) p. C99.
81. *T. Ashley* et al.: Semicond. Sci. Technol., **8** (1993) p. S386.
82. *Z. Djuric, J. Piotrowski:* Electron. Lett., **26** (1990) p. 1689.
83. *Z. Djuric, J. Piotrowski:* Proc. SPIE, **1540** (1992) p. 1540.
84. *R.A. Wood, N.A. Foss:* Laser Focus World, June 1993, p. 101.
85. *R.C. Jones:* Advances in Electronics, **5** (1953) p. 1.
86. *R.W. Whatmore:* Rep. Prog. Phys., **49** (1986) p. 1335.
87. *R.W. Whatmore:* Ferroelectrics, **118** (1991) p. 241.
88. *R. Watton:* Ferroelectrics, **91** (1989) p. 87.
89. *J.M. Lloyd:* Thermal Imagimg Systems. Plenum Press, New York 1975.
90. *T.C. Herman, I. Melngailis*: in: Applied Solid State Science (*R. Wolfe* – ed). Academic Press, New York 1974, p. 1.
91. *J.T. Longo* et al.: IEEE Trans. Electron Devices, **ED-25** (1978) p. 213.